Journal of Surface Engineered Materials and Advanced Technology, 2026, 16(4), 39-56
https://www.scirp.org/journal/jsemat
ISSN Online: 2161-489X
ISSN Print: 2161-4881

Analytical Modeling of Thermomagnetic Effects on the Dynamic Transport of Minority Carriers in an n⁺-p-p⁺ Silicon Solar Cell under Modulated Illumination

Sada Traore*, Seydou Faye, Landing Diatta, Moustapha Thiame

Laboratory of Semiconductor and Solar Energy, Cheikh Anta Diop University, Dakar, Senegal
Email: *sadatraore59@yahoo.fr

How to cite this paper: Traore, S., Faye, S., Diatta, L. and Thiame, M. (2026) Analytical Modeling of Thermomagnetic Effects on the Dynamic Transport of Minority Carriers in an n⁺-p-p⁺ Silicon Solar Cell under Modulated Illumination. *Journal of Surface Engineered Materials and Advanced Technology*, **16**, 39-56.
https://doi.org/10.4236/jsemat.2026.164004

Received: August 22, 2026
Accepted: September 19, 2026
Published: September 22, 2026

Abstract

This work develops an analytical model for the dynamic transport of minority electrons in the base of an n⁺-p-p⁺ silicon solar cell subjected to a transverse static magnetic field at different temperatures and to modulated polychromatic illumination. The continuity equation is solved in the harmonic regime by accounting for optical generation, bulk and interface recombination, and the thermomagnetic dependence of the diffusion coefficient. The frequency response is described through the complex diffusion length, the complex minority-carrier density, and the complex photocurrent. At 300 K, the zero-field diffusion coefficient is 34.90 cm²/s, whereas the thresholds corresponding to 1% and 10% reductions in Dn are 0.745 T and 2.469 T, respectively. For a carrier lifetime of 1 µs, the characteristic frequency fc is 159.15 kHz. At this frequency, the diffusion-length magnitude is 84.1% of its quasi-static value and its phase is −22.5˚. However, the change in internal transport is not transmitted proportionally to the photocurrent: at 300 K and $f = f_c$, a 1% reduction in D_n at 0.745 T produces only a 0.0858% attenuation of the photocurrent, whereas the 1% electrical threshold is reached near 2.61 T. Increasing temperature reduces mobility and shifts the magnetic thresholds toward higher fields. The indicators C_{TM}, S_B and I_{TM} respectively characterize the normalized magnetic response, define the electrical thresholds and isolate the thermomagnetic interaction relative to 300 K.

Keywords

Silicon Solar Cell, Minority Carriers, Magnetic Field, Temperature, Modulated Illumination, Complex Photocurrent

1. Introduction

Improving and characterizing photovoltaic cells requires a precise understanding of the mechanisms governing the generation, diffusion, recombination, and collection of photogenerated carriers. In an n^+-p-p^+ silicon solar cell, the electrical response depends notably on minority-electron transport in the p-type base, carrier lifetime, and surface recombination velocities [1]-[4]. Within the transverse magnetodiffusion approximation, an applied magnetic field reduces the diffusion coefficient along the carrier-collection direction through the Lorentz-force contribution to transport [5]-[7].

Environmental fields, including the geomagnetic field of approximately 25 - 65 μT [8], remain far below the tesla-scale fields produced in laboratory facilities. Accordingly, extending the present study to 5 T constitutes a theoretical exploration of strong magnetic perturbations rather than a representation of ordinary photovoltaic operating conditions.

Under modulated illumination, the excess minority-carrier density is described by a complex amplitude, whose magnitude characterizes the oscillating carrier population and whose phase represents its delay relative to the excitation [9]-[11]. Frequency-domain analysis distinguishes a quasi-static regime from a dynamic regime characterized by amplitude attenuation and increasing phase lag. Previous studies have investigated magnetic-field effects on carrier diffusion under steady-state or frequency-dependent conditions [12]-[14], as well as the combined influence of temperature and magnetic field [15] [16]. However, the quantitative relationship between changes in internal transport properties and the resulting electrical response remains insufficiently clarified.

The present work develops an analytical framework linking the thermomagnetic diffusion coefficient to the complex diffusion length, spatial profiles of the complex minority-carrier density, and complex photocurrent of an n^+-p-p^+ silicon solar cell under modulated polychromatic illumination. It examines how temperature and magnetic field affect the amplitude, phase, and characteristic transition frequencies of the response, while distinguishing transport-based magnetic thresholds from photocurrent-based thresholds. These thresholds are defined using prescribed relative-change criteria rather than assumed experimental detection limits.

Building on the internal-transport analysis reported in Ref. [15], the methodological contribution of the present study lies in quantifying the propagation of thermomagnetic effects from carrier transport to the collected photocurrent. Three indicators are introduced: C_{TM}, which quantifies the normalized magnetic response; S_B, which represents the relative photocurrent reduction used to define operational magnetic thresholds; and I_{TM}, which isolates the thermal modification of the relative magnetic response with respect to the reference temperature T_{ref} = 300 K. Together, these indicators demonstrate that a given relative change in the diffusion coefficient does not necessarily produce an equivalent relative change in the collected photocurrent.

2. Theory and Modeling

2.1. Structure of the n^+-p-p^+ Solar Cell

The model developed in this work is based on the structure shown in **Figure 1**. The device is a monofacial silicon solar cell consisting of a thin, heavily doped n^+ emitter, a p-type base of thickness H, and a rear p^+ region acting as a back-surface field (BSF). The n^+/p junction separates the photogenerated electron-hole pairs; the p/p^+ transition produces an internal electric field that drives minority electrons toward the collecting junction and thereby reduces their recombination at the rear surface [17]. The origin $x = 0$ is located at the edge of the space-charge region on the base side, and $x = H$ at the p/p^+ interface. Polychromatic illumination is incident on the front surface (n^+ side). The uniform static magnetic field B forms an angle θ with the main carrier-diffusion direction (x axis). The adopted model is one-dimensional and assumes low-level injection, a homogeneous quasi-neutral base, and physical parameters (mobility, lifetime, and diffusion coefficient) that are uniform across the base thickness.

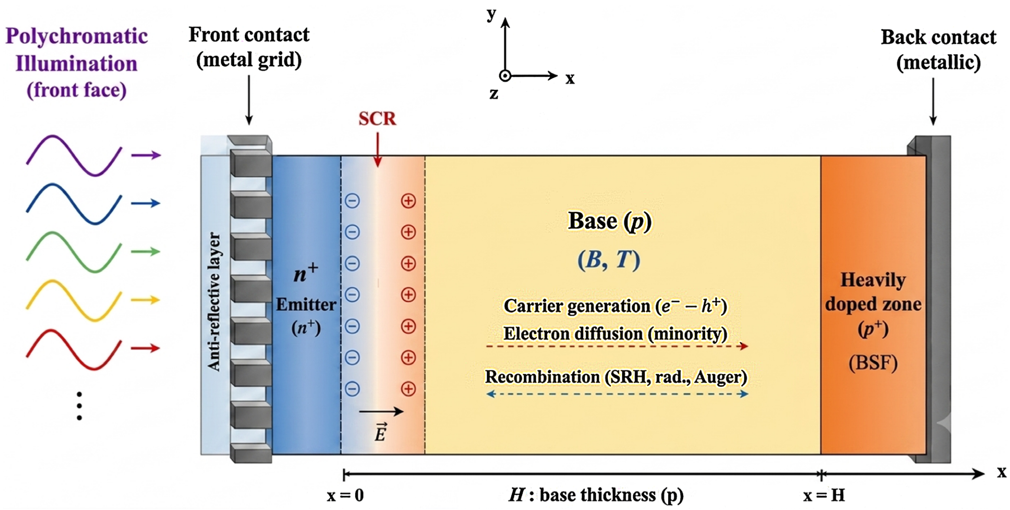

Figure 1. Structure of the monofacial n^+-p-p^+ silicon solar cell.

This representation brings together the three coupled physical mechanisms in the base: electron-hole pair generation under polychromatic illumination, diffusion toward the collecting junction, and bulk (Shockley-Read-Hall, radiative, and Auger) [18] and surface recombination. The pair (B, T) acts directly on diffusive transport, whereas the p^+ back-surface field affects the recombination boundary condition at $x = H$. This structure provides the basis for the mathematical model developed in the remainder of this section.

2.2. Dynamic Continuity Equation for Minority Carriers

In the frequency-domain dynamic regime, the continuity equation coupling the diffusion, generation, and recombination of minority carriers (electrons) in the p-type base is written as:

$$\frac{\partial \delta_n(x,t)}{\partial t} = D_n(B,T)\frac{\partial^2 \delta_n(x,t)}{\partial x^2} - \frac{\delta_n(x,t)}{\tau n} + G(x,t) \quad (1)$$

where $\delta_n(x,t)$ and $G(x,t)$ respectively represent the excess minority-electron density in the base and the overall generation rate of carriers under polychromatic illumination. They are given by the following relations:

$$\delta_n(x,t) = \delta_n(x)\cdot \mathrm{e}^{j\omega t} \text{ et } G(x,t) = g(x)\cdot \mathrm{e}^{j\omega t} \quad (2)$$

where $\delta(x)$ and $g(x)$ denote the spatial component and $\mathrm{e}^{i\omega t}$ the temporal component.

For this type of solar cell, the spatial component of the minority-carrier generation rate is given by Equation (3):

$$g(x) = n\cdot \sum_{k=1}^{3} a_i \cdot \mathrm{e}^{-b_i x} \quad (3)$$

where a_i and b_i are tabulated coefficients of solar radiation that depend on the wavelength-dependent absorption coefficient of silicon under AM 1.5.

n : represents the illumination level expressed in suns. It relates the experimental illumination level to the AM 1.5 reference illumination level; x: denotes depth in the base, measured from the emitter junction ($x = 0$) to the rear surface ($x = H$). This generation model provides the source term in Equation (1); the diffusion coefficient D_n, which governs transport, must now be characterized as a function of magnetic field, temperature, and modulation frequency.

2.3. Thermomagnetic Transport Model

2.3.1. Thermomagnetic Diffusion Coefficient

The temperature-dependent diffusion coefficient is given by the Einstein relation:

$$D_n(T) = \mu_n(T)\times \frac{k_B\cdot T}{q} \quad (4)$$

where k_B is the Boltzmann constant, q is the elementary charge, and $\mu_n(T)$ is the electron mobility in the base. Over the temperature range studied, its thermal dependence is represented by Equation (5), in accordance with the parameterization of silicon transport properties proposed by Jacoboni *et al.* [19]. At the reference temperature T_{ref} = 300 K, μ_n (300 K) = 1350 cm^2/V·s is adopted for lightly doped silicon [19] [20].

$$\mu_n(T) = \mu_n(T_{ref})\left(\frac{T}{T_{ref}}\right)^{-2.42} \quad (5)$$

Under a static magnetic field B, the Lorentz force deflects minority-carrier trajectories and reduces their longitudinal diffusion coefficient. Under steady conditions, this reduction is expressed as:

$$D_n(B,T) = \frac{D(T)}{1+\left[\mu(T)B\right]^2} \quad (6)$$

This relation shows that the relative magnetic suppression of diffusion increases with the dimensionless parameter $\mu(T)B$. Here, the magnetic field is perpendicular to the main diffusion direction, corresponding to $\theta = \pi/2$, so that $B_{\perp} = B$.

Magnetic-field effects are represented by a one-dimensional scalar approximation for diffusion along the carrier-collection direction. This model captures the reduction of longitudinal transport but neglects off-diagonal Hall terms, transverse carrier redistribution, Hall electric fields, and finite-width edge effects. The results should therefore be interpreted within this restricted approximation rather than as a complete tensorial description of magnetotransport [7] [19] [20].

2.3.2. Coupled Thermomagnetic Diffusion Length

The complex diffusion length under magnetic field B and temperature T is given by:

$$L_{\omega}^{*}(\omega, B, T) = \sqrt{\frac{D_n(B,T)\cdot\tau_n}{1 + j\tau_n\omega}} \tag{7}$$

This expression highlights the coupling among the thermal, magnetic, and frequency effects considered in the present model. Temperature acts on electron mobility and the diffusion coefficient, the magnetic field reduces longitudinal transport, and the modulation frequency produces attenuation and phase lag through the factor $\omega\tau_n$. In all simulations, the minority-carrier lifetime is fixed at $\tau_n = 1.0\ \mu\text{s}$ for every temperature and magnetic-field strength; consequently, $f_c = [2\pi\tau_n]^{-1} = 159.15\ \text{kHz}$ remains constant over 280 - 360 K. No temperature- or magnetic-field-dependent lifetime law is assumed in this work.

2.4. Analytical Solution for Minority-Carrier Transport

2.4.1. General Solution of the Diffusion Equation

The general solution of continuity Equation (1) for the excess minority-carrier density in the base as a function of depth x is:

$$\delta(x,\omega,B,T) = A\cosh\left(\frac{x}{L_{\omega}^{*}(\omega,B,T)}\right) + B\sinh\left(\frac{x}{L_{\omega}^{*}(\omega,B,T)}\right) + \sum_{i=1}^{3}\beta_i\cdot e^{-b_i x} \tag{8}$$

where the coefficients βi are given by:

$$\beta_i = -\frac{na_i\cdot L_{\omega}^{*}(B,T)^2}{D_n(B,T)\left[\left(b_i\cdot L_{\omega}^{*}(\omega,B,T)\right)^2 - 1\right]} \tag{9}$$

A and B are two integration constants determined by the boundary conditions at the n^+/p junction and the rear p/p^+ interface.

2.4.2. Boundary Conditions

At the n^+/p junction, continuity between the diffusion current and the current crossing the junction imposes:

$$\left.\frac{\delta(x,\omega,B,T)}{\partial x}\right|_{x=0} = \frac{S_f}{D_n(B,T)}\delta(0,\omega,B,T) \tag{10}$$

where S_f is the junction recombination velocity [21] [22]. This velocity equals the sum of the recombination velocity associated with the external load ($S_{fj} = 10^j$) and the intrinsic recombination velocity S_{f0}, an effective emitter-base interface recombination velocity. It accounts for both interfacial recombination mechanisms and electron extraction by the junction.

At the rear p/p⁺ interface, the recombination boundary condition is:

$$\left.\frac{\delta(x,\omega,B,T)}{\partial x}\right|_{x=H} = -\frac{S_b}{D_n(B,T)}\delta(H,\omega,B,T) \tag{11}$$

where S_b is the back-surface recombination velocity. A low S_b value corresponds to effective passivation and efficient action of the p^+ back-surface field [23].

2.5. Complex Photocurrent

The thermomagnetically coupled frequency-dependent photocurrent density is obtained from the diffusion current evaluated at the junction:

$$J_{ph}(\omega,B,T) = q\cdot D_n(B,T)\left.\frac{\partial\delta_n(x,\omega,B,T)}{\partial x}\right|_{x=0} \tag{12}$$

Its magnitude and phase are respectively given by:

$$\left|J_{ph}(\omega,B,T)\right| \qquad \varphi_J = \arg\left(J_{ph}(\omega,B,T)\right) \tag{13}$$

These two quantities, the magnitude and phase of the complex photocurrent, are the principal observables of the parametric study presented in the following section. The effects of magnetic field, temperature, and modulation frequency on minority-carrier transport and collection are examined successively through numerical simulations of the model established above.

3. Results and Discussion

The numerical simulations presented in this section are based on the analytical model established in Section 2 and cover an external magnetic-field range from 0 to 5 T. This range encompasses the environmental micromagnetic reference regime, the critical transport regime in which magnetoresistance significantly alters carrier-collection dynamics, and the intense macromagnetic regime associated with specialized laboratory characterization and certain physically confined applications [24] [25].

Unless otherwise stated, all simulations use a base thickness $H = 0.020$ cm, a fixed minority-carrier lifetime $\tau_n = 1.0 \times 10^{-6}$ s, a total effective junction recombination velocity $S_f = 6.0 \times 10^6$ cm·s^{-1}, a rear-surface recombination velocity $S_b = 200$ cm s^{-1}, and an illumination level $m = 1$ sun. The polychromatic generation coefficients are $a_1 = 6.13 \times 10^{20}$, $a_2 = 0.54 \times 10^{20}$, and $a_3 = 0.0991 \times 10^{20}$ cm^{-3}·s^{-1}, with $b_1 = 6630$, $b_2 = 1000$, and $b_3 = 130$ cm^{-1}, respectively. These values are consistent with the optical-generation and boundary-condition parameterizations adopted in Refs. [15] [21]-[23]. The numerical calculations use the total effective value of S_f directly; the decomposition $S_f = S_{f0} + S_{fj}$ and the load-dependent term S_{fj} are not varied independently in the simulations.

3.1. Effects of Magnetic Field and Temperature on the Diffusion Coefficient $D_n(B, T)$

To quantify the influence of the field on diffusive transport, the relative reduction in the diffusion coefficient is defined as:

$$R_D(B,T)=\frac{D_0(T)-D_n(B,T)}{D_0(T)}\times 100 \quad (14)$$

At 300 K, the Einstein relation gives a zero-field diffusion coefficient D_n(300 K) = 34.90 cm²·s⁻¹ for an electron mobility of 1350 cm²·V⁻¹·s⁻¹. Substitution into $D_n(B,T)=D(T)\Big/\left(1+\left[\mu(T)B\right]^2\right)$ shows that fields below 100 mT modify electron diffusion only very weakly (Table 1). At 50 mT, for example, D_n decreases only from 34.9002 to 34.8986 cm²·s⁻¹, corresponding to a reduction of 0.00456%. The conventional 1% threshold is reached at B threshold = 0.74447 T. The decrease then becomes more noticeable, reaching 1.79% at 1 T, 6.79% at 2 T, and 31.30% at 5 T.

Table 1. Values of D_n and R_D at different magnetic-field strengths at T = 300 K.

B (T)	D_n (cm²·s⁻¹)	R_D (%)	Interpretation
0	34.9002	0	Reference
0.01	34.9001	0.000182	Negligible effect
0.04	34.8992	0.002916	Negligible effect
0.05	34.8986	0.004556	Negligible effect
0.1	34.8938	0.018222	Very weak effect
0.5	34.7419	0.453558	Reduction below 1%
0.74447	**34.5512**	**1**	**1% modification threshold**
1	34.2755	1.789879	Modified transport
2	32.5289	6.794669	Intermediate modification
5	23.9761	31.300988	Strong perturbation at 31.3%

The value $D_n(0)$ = 34.90 cm²·s⁻¹ obtained at 300 K differs by only 0.285% from the value of 35 cm²·s⁻¹ adopted by Combari *et al.* [26], indicating satisfactory zero-field agreement. Under a magnetic field, however, the comparison reveals a substantial quantitative divergence. At 50 mT, the present model predicts a relative diffusion-coefficient reduction of only $R_D = 4.56 \times 10^{-3}$%, whereas some theoretical and experimental studies report a much stronger decrease in short-circuit current within this field range [6] [26]. This divergence cannot be explained by the small difference between 34.90 and 35 cm²·s⁻¹. It may arise from additional mechanisms not represented by the sole factor $1/[1+(\mu_n B)^2]$, differences in whether the applied field is static or alternating, experimental conditions, or the treatment of mobility and magnetic-field units. The present results should therefore be interpreted within the validity domain of the classical magnetodiffusion model. Their extrapolation to the overall electrical response of a photovoltaic module requires experimental validation under a controlled field.

Irrespective of this divergence from some electrical responses reported in the literature, three magnetodiffusion regimes can be distinguished from the R_D values listed in Table 1.

The range $0 \le B < 0.745$ T corresponds to a change in D_n below 1% according to the adopted criterion; it broadly includes the geomagnetic field, approximately 25 - 65 μT [27], and local fields produced by many permanent magnets. The range $0.745 \le B < 2.469$ T corresponds to a to a model-defined transport modification between the adopted 1% and 10% criteria; such fields can be generated by powerful electromagnets or superconducting magnets, including the static fields of 1.5 and 3 T commonly used in magnetic resonance imaging (MRI) systems [28]. Finally, $2.469 \le B \le 5$ T represents a strong-perturbation regime in which the reduction in D_n reaches approximately 31.3% at 5 T. This range corresponds to specialized laboratory characterization rather than ordinary photovoltaic operation; its technical feasibility is demonstrated by laboratory superconducting magnets capable of producing continuous fields well above 5 T and exceeding 45 T in the most powerful research facilities [24] [25].

Figure 2 shows the minority-electron diffusion coefficient and its relative reduction R_D as functions of magnetic field for five temperatures between 280 and 360 K.

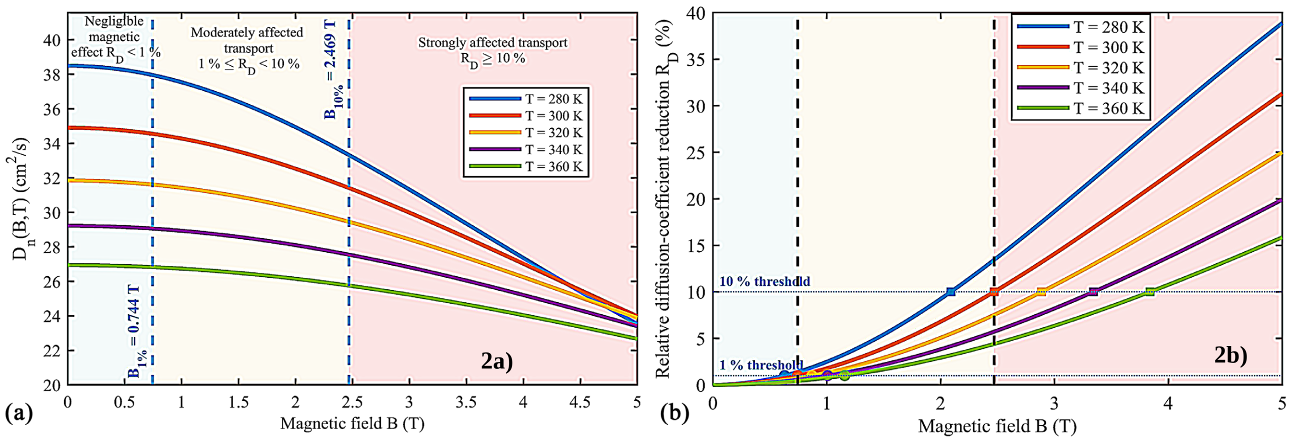

Figure 2. Minority-electron diffusion coefficient and relative reduction R_D as functions of magnetic field for $280 \le T \le 360$ K.

For all temperatures considered, D_n decreases as B increases, in agreement with $D_n(B,T) = D_0(T) \big/ \left[1+\left(\mu_n(T)B\right)^2\right]$. This decrease reflects the greater deflection of minority carriers by the Lorentz force and the resulting reduction in their longitudinal diffusive transport. Within the adopted model, the diffusion coefficient also decreases with temperature because the thermal decrease in mobility, described by $\mu_n(T) \propto T^{-2.42}$, dominates the increase in the thermal factor $k_B T/q$.

At the reference temperature of 300 K, the three regimes previously defined from R_D are clearly visible in Figure 2(b). For $0 \le B < 0.745$ T, R_D remains below

1%, so the magnetic influence may be considered negligible under the adopted criterion. Between 0.745 and 2.469 T, the reduction ranges from 1% to 10%, corresponding to a model-defined modification of minority-carrier transport exceeding the adopted 1% criterion. Finally, for 2.469 ≤ B ≤ 5 T, the reduction exceeds 10% and reaches approximately 31.3% at 5 T, characterizing a strong magnetic-perturbation regime.

The thresholds are nevertheless temperature dependent. Their shift toward higher fields as temperature increases results from the decrease in electron mobility. Thus, the 10% threshold rises from approximately 2.09 T at 280 K to 3.84 T at 360 K. Conversely, at a given field, the relative reduction is greater at lower temperatures. The convergence of the curves at high fields results from competition between the higher initial D_0 at low temperatures and the increased magnetic sensitivity associated with greater mobility.

This first analysis identifies the conditions under which the internal parameter D_n is affected. To determine how this modification propagates to the dynamic response, the complex diffusion length, which combines D_n with carrier lifetime and modulation frequency, is examined next.

3.2. Frequency Behavior of the Complex Diffusion Length

Figure 3 presents the frequency dependence of the magnitude and phase of the complex diffusion length for different magnetic-field strengths at T = 300 K and τ_n = 1 μs. The characteristic frequency associated with this lifetime is f_c = 159.15 kHz.

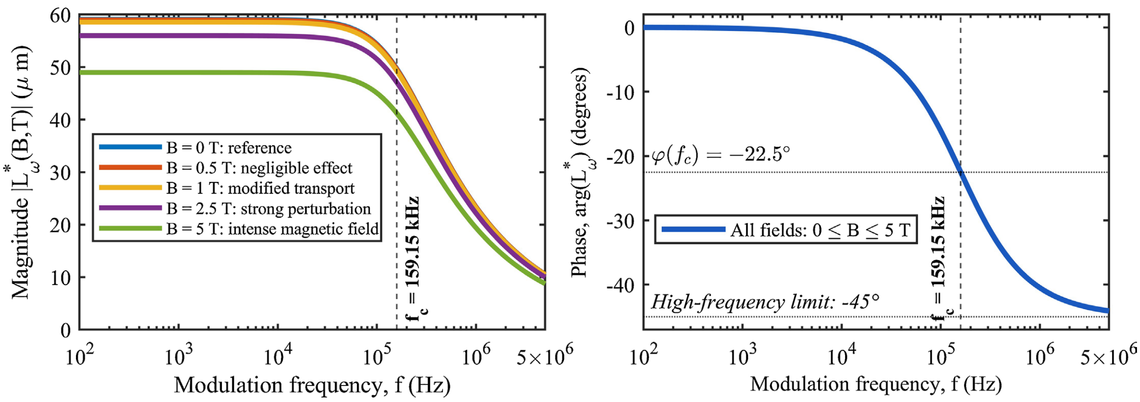

Figure 3. Magnitude and phase of the complex diffusion length as functions of frequency for different B values at T = 300 K and τ_n = 1 μs.

In the low-frequency regime, the magnitude approaches its quasi-static value $\sqrt{D_n(B,T)\tau_n}$. Its progressive decrease with increasing magnetic field results from the field-induced reduction in the diffusion coefficient of minority carriers. At B = 5 T, the magnitude is approximately 17.1% lower than its zero-field value. Near the characteristic frequency f_c = 159.15 kHz, the magnitude begins to decrease significantly and reaches $2^{-1/4}$, or approximately 84.1% of its quasi-static value. At higher frequencies, it follows the asymptotic behavior $|L_\omega^*| \propto f^{-1/2}$, indicating a progressive reduction in the dynamic penetration depth of minority carriers.

The phase evolves from nearly 0˚ in the quasi-static regime to −22.5˚ at $f = f_c$ and then approaches −45˚ in the high-frequency asymptotic regime. Assuming that the minority-carrier lifetime is independent of magnetic field, the phase has no explicit dependence on B; the phase curves associated with the different magnetic-field strengths therefore overlap. Within the limits of the present model, the magnetic field modifies the magnitude of the complex diffusion length without changing its characteristic frequency or phase response. The diffusion length describes a transport scale but does not, by itself, specify the actual carrier distribution in the base. The next step therefore incorporates polychromatic generation and the boundary conditions to analyze the spatial density profiles.

3.3. Magnitude and Phase of the Carrier Density

The combined analysis of the magnitude and phase of the complex minority-carrier density (**Figure 4**) fully characterizes its dynamic response. The magnitude describes attenuation of the photogenerated population through diffusion and recombination, whereas the phase quantifies the carrier delay relative to the modulated optical excitation. This analysis identifies the transition between the quasi-static and dynamic regimes and assesses the influence of temperature and magnetic field on carrier transport and collection at T = 300 K and B = 1 T.

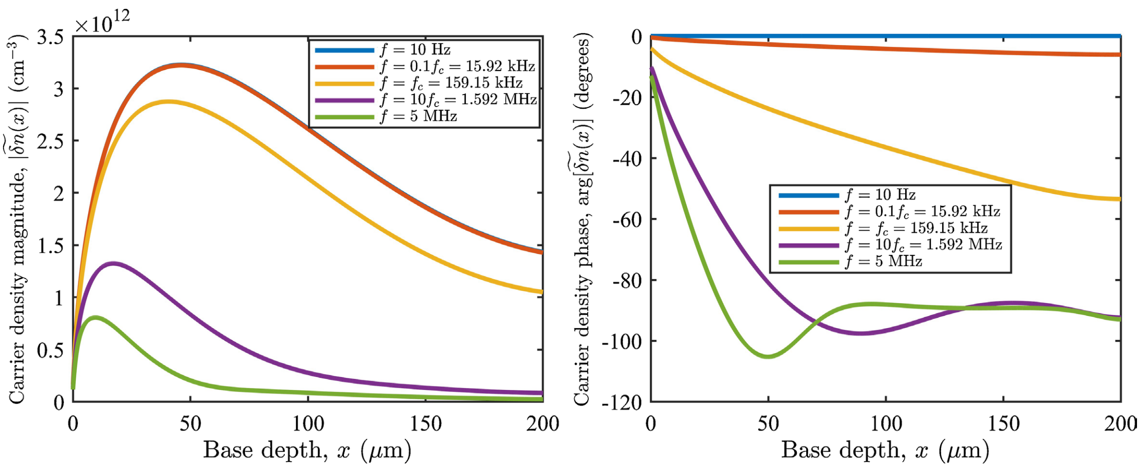

Figure 4. Magnitude and phase of the complex minority-electron density at different modulation frequencies, for T = 300 K and B = 1 T.

Under front-side polychromatic illumination, the density magnitude rises rapidly from the junction, reaches a maximum at a depth of approximately 40 - 50 µm, and then decreases toward the rear surface. The low density near the junction results from the high recombination-velocity value, which limits carrier accumulation in this region.

In the quasi-static regime, the profiles at 10 Hz and 0.1fc nearly coincide, showing that the carriers can follow the illumination modulation. When the frequency reaches f_c = 159.15 kHz, the amplitude begins to decrease noticeably and a substantial spatial phase lag appears. For $f \gg f_c$, the density is strongly attenuated and becomes more localized near the generation region because the carriers no longer have sufficient time to diffuse deeply into the base.

The phase, which is nearly zero at low frequency, becomes progressively more negative as frequency and depth increase. This behavior reflects the delay of the carrier response relative to the optical excitation. At high frequencies, nonmonotonic phase variations result from interference among the complex contributions of the homogeneous solution, polychromatic generation, and the boundary conditions.

These profiles reveal the internal dynamics of the base. To relate these dynamics to a directly usable electrical quantity, the remainder of the analysis focuses on the junction photocurrent and its normalization relative to the zero-field case.

3.4. Normalized Magnetic Response C_{TM} and Threshold Indicator S_B

To quantify the specific influence of the magnetic field on the dynamic response of the cell independently of its absolute photocurrent level, a relative magnetic-response factor is defined as:

$$C_{TM}(T,B,f) = \frac{\left|J_{ph}(T,B,f)\right|}{\left|J_{ph}(T,0,f)\right|} \tag{15}$$

This relative factor is interpreted as follows:

- $C_{TM} = 1$: no magnetic effect on the amplitude
- $C_{TM} < 1$: photocurrent attenuation
- $C_{TM} > 1$: photocurrent enhancement

A value of unity corresponds to a photocurrent that is insensitive to the field, whereas $C_{TM} < 1$ denotes attenuation and $C_{TM} > 1$ denotes enhancement.

This factor is related to the signed sensitivity by:

$$S_B(T,B,f) = 100\left(1 - C_{TM}(T,B,f)\right) \tag{16}$$

$S_B > 0$ indicates photocurrent attenuation under magnetic field, whereas $S_B < 0$ indicates an increase.

Because these two quantities are redundant, C_{TM} is used to represent the normalized response, whereas S_B is used only to define the operational thresholds $B_{J,1\%}$ and $B_{J,10\%}$. These thresholds apply to the photocurrent and may differ substantially from those derived from D_n.

The electrical thresholds $B_{J,1\%}$ and $B_{J,10\%}$ are operational, model-defined criteria obtained from $|S_B(T, B, f)| = 1\%$ and $|S_B(T, B, f)| = 10\%$, respectively. They are not experimental detection limits unless a measurement uncertainty and instrumental resolution are explicitly specified.

Figure 5 and Figure 6 respectively show the magnetic-field and frequency dependence of the normalized magnetic response.

Figure 5 shows that C_{TM} starts at unity for $B = 0$ and progressively decreases with field strength; the field therefore slightly attenuates the photocurrent magnitude in the present model. The departure from unity is more pronounced at low temperature, consistent with the higher electron mobility and increased sensitivity of D_n. It also increases in the dynamic regime, thereby lowering the field required to reach a given level of electrical variation.

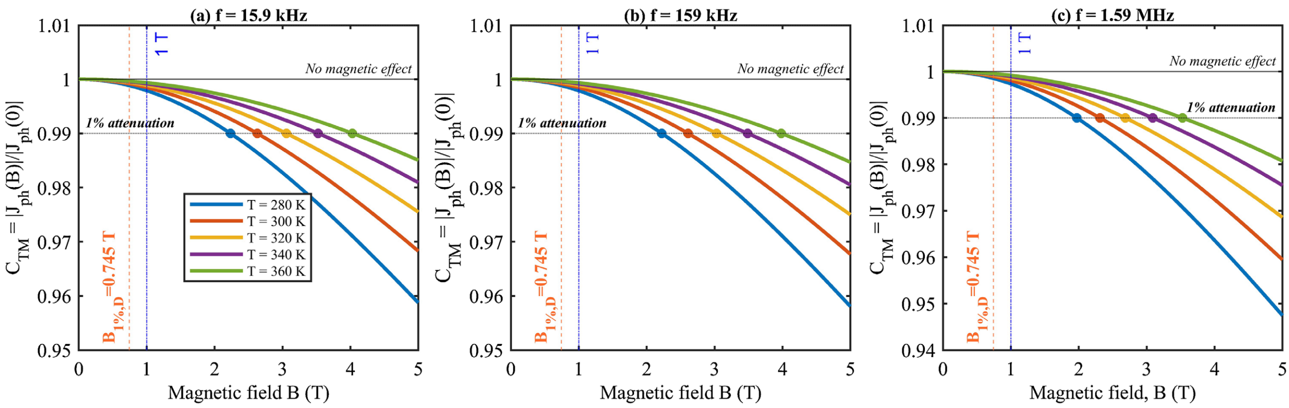

Figure 5. Normalized magnetic response C_{TM} as a function of B at $0.1f_c$, f_c, and $10f_c$ for different temperatures.

A key result is that $B_{1\%,D}$ = 0.745 T, defined by a 1% reduction in D_n at 300 K, produces only a 0.0858% reduction in $|J_{ph}|$ at $f = f_c$. At 300 K, the electrical threshold $|S_B|$ = 1% is approximately 2.61 T at f_c. Geometry, generation, and collection conditions therefore filter out part of the change in the diffusion coefficient.

Using the numerical parameter set stated above, the electrical threshold $B_{J,1\%}$ is obtained by solving $|S_B(300\text{ K}, B, f_c)|$ = 1%, which yields approximately 2.61 T. This value is specific to the adopted base thickness, lifetime, optical-generation model, recombination velocities, illumination level, and operating frequency; it is not a universal magnetic threshold for silicon solar cells.

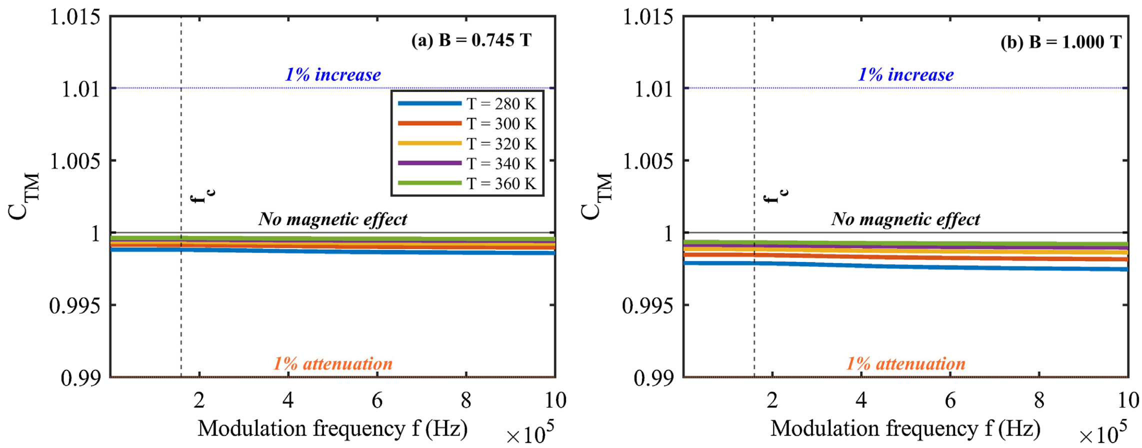

Figure 6. Frequency dependence of CTM for B = 0.745 T and B = 1 T at different temperatures.

Figure 6 confirms that, for B = 0.745 and 1 T, C_{TM} remains very close to unity throughout the studied frequency range. The effect is nearly negligible in the quasi-static regime and becomes slightly more visible when f exceeds fc, although it does not reach 1% over this magnetic-field interval. The separation of the curves with temperature shows that normalization by $J_{ph}(T, 0, f)$ does not remove the thermal dependence of magnetic sensitivity. This residual dependence motivates the introduction of I_{TM}.

3.5. Thermomagnetic Interaction I_{TM}

To isolate the thermal modification of the relative magnetic response, the following indicator is defined with respect to $T_{ref} = 300$ K:

$$I_{TM}(T,B,f) = 100\left[\frac{C_{TM}(T,B,f)}{C_{TM}(T_{ref},B,f)} - 1\right] \tag{17}$$

At identical magnetic field and frequency, this indicator compares the relative field effect at temperature T with that obtained at 300 K.

The sign of I_{TM} indicates whether the relative magnetic attenuation is weaker or stronger than in the reference case.

By construction, I_{TM} is zero at the reference temperature and in the absence of a magnetic field. A nonzero value indicates that temperature modifies the relative effect of the magnetic field on the photocurrent. Joint consideration of C_{TM} and I_{TM} therefore distinguishes a simple magnetic variation in photocurrent from a genuine thermomagnetic interaction in the dynamic response of the cell.

Thus, C_{TM} describes the normalized magnetic response, S_B provides a directly interpretable threshold criterion, and I_{TM} reveals the intrinsic thermal dependence of this effect.

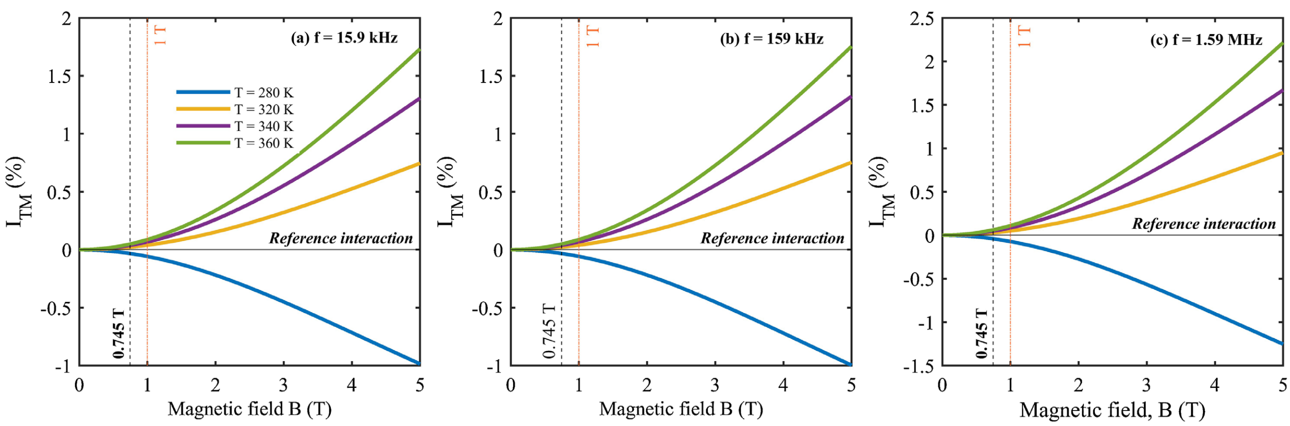

Figure 7. Thermomagnetic interaction I_{TM} as a function of B relative to $T_{ref} = 300$ K for three frequency regimes.

Figure 7 verifies the normalization properties: I_{TM} is zero at $B = 0$ for every temperature and identically zero at 300 K. For $T < 300$ K, I_{TM} is negative, meaning that C_{TM} is below its reference value and the relative magnetic attenuation is stronger. For $T > 300$ K, I_{TM} becomes positive: the thermal decrease in mobility makes the photocurrent relatively less sensitive to the field. The magnitude of the interaction increases with B and becomes more noticeable in the dynamic regime.

3.6. Mapping of the Thermomagnetic Interaction

To summarize these observations in a single representation, Figure 8 maps the thermomagnetic interaction indicator I_{TM} in the (B, T) plane at the characteristic frequency f_c = 159.15 kHz.

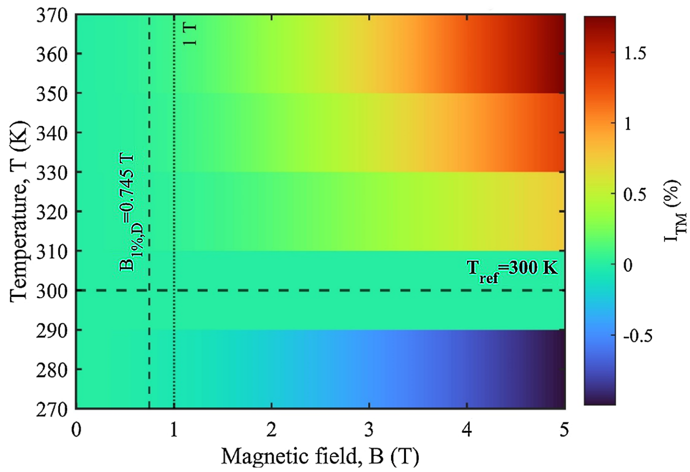

Figure 8. Map of the thermomagnetic interaction I_{TM} in the (B, T) plane at f = f_c = 159.15 kHz.

This map concisely confirms the trends identified in **Figure 7**: I_{TM} is zero along the T = 300 K isotherm (central green band), increases with B above this isotherm (yellow-orange to red shades, indicating weaker relative photocurrent attenuation), and decreases below it (blue shades, indicating stronger relative attenuation). The steepest gradient appears in the upper-right corner of the map (high T and high B), where the mobility difference between T and T_{ref} is greatest and its effect on the term $\mu_n(T)B$ is most pronounced. This two-dimensional representation therefore provides a rapid means of anticipating, at a given frequency, the direction and magnitude of the expected thermomagnetic interaction for a specified pair (B, T), before consulting the detailed curves in **Figures 5-7**.

3.7. Numerical Summary of the Thermomagnetic Indicators

Table 2 summarizes the numerical values of R_D, C_{TM}, S_B, and I_{TM}, together with the magnitude and phase of the photocurrent, for three representative magnetic fields ($B \approx 0$ T, represented here by 0.001 T as a quasi-zero reference; B = 0.745 T, corresponding to the $B_{1\%}$ threshold; and B = 1 T) and for the five temperatures considered in the preceding figures.

The table quantitatively confirms all the qualitative trends identified in the preceding subsections. At a quasi-zero field (B = 0.001 T), R_D is negligible (of the order of 10^{-6}%), C_{TM} is numerically indistinguishable from unity at the displayed precision, and I_{TM} remains of the order of 10^{-7} - 10^{-8}%, confirming the internal numerical consistency of the model. For the two nonzero fields (0.745 and 1 T), both R_D and S_B decrease monotonically with increasing temperature. At B = 1 T, for example, R_D decreases from 2.48% at 280 K to 0.75% at 360 K, while S_B decreases from 0.212% to 0.066% over the same interval. This confirms that the magnetic sensitivity of transport decreases as temperature rises, in agreement

Table 2. Summary of the thermomagnetic indicators (R_D, C_{TM}, S_B, and I_{TM}) and the complex photocurrent (magnitude and phase) as functions of temperature T for three magnetic-field strengths (≈ 0, 0.745, and 1 T) at the characteristic frequency f_c = 159.15 kHz.

B (T)	T (K)	R_D (%)	C_{TM}	S_B (%)	I_{TM} (%)	$\|J_{ph}\|$ (mA·cm^{-2})	φJ_{ph} (°)
0.001	280	2.545×10^{-6}	1	2.144×10^{-7}	-5.902×10^{-8}	26.655	−3.9064
	300	1.823×10^{-6}	1	1.554×10^{-7}	0	26.434	−3.9455
	320	1.334×10^{-6}	1	1.151×10^{-7}	4.031×10^{-8}	26.227	−3.9849
	340	9.944×10^{-7}	1	8.686×10^{-8}	6.855×10^{-8}	26.032	−4.0241
	360	7.541×10^{-7}	1	6.663×10^{-8}	8.878×10^{-8}	25.847	−4.0628
0.745	280	1.3929	0.99882	0.11821	−0.03240	26.623	−3.9118
	300	1.0014	0.99914	0.08584	0	26.412	−3.9497
	320	0.7347	0.99936	0.06366	0.02220	26.211	−3.9881
	340	0.5489	0.99952	0.04808	0.03779	26.020	−4.0266
	360	0.4168	0.99963	0.03691	0.04898	25.838	−4.0648
1.000	280	2.4818	0.99788	0.21184	−0.05786	26.598	−3.9161
	300	1.7899	0.99846	0.15407	0	26.394	−3.9530
	320	1.3160	0.99886	0.11437	0.03976	26.197	−3.9908
	340	0.9846	0.99914	0.08645	0.06772	26.010	−4.0287
	360	0.7485	0.99934	0.06639	0.08782	25.830	−4.0664

with Figure 2 and Figure 5. Correspondingly, C_{TM} approaches unity as T increases, indicating weaker magnetic attenuation of the photocurrent at higher temperatures.

The I_{TM} indicator faithfully reproduces the behavior observed in Figure 7: it is zero by construction at 300 K, negative at 280 K, and positive at 320, 340, and 360 K, with a magnitude that increases with magnetic field. The ranges are −0.03% ≤ I_{TM} ≤ 0.06% at B = 0.745 T and −0.06% ≤ I_{TM} ≤ 0.09% at B = 1 T. The photocurrent magnitude $|J_{ph}|$ decreases only slightly as both B and T increase (from 26.655 to 25.830 mA·cm^{-2} over the entire table), confirming that most of the photocurrent variation originates from temperature rather than magnetic field. Indeed, the field effect remains below 0.22% over the investigated range $B \leq 1$ T. Finally, the photocurrent phase becomes systematically more negative as temperature increases (from −3.91° at 280 K to −4.06° at 360 K at fixed field), indicating a slight additional delay in the dynamic response of the cell at higher temperatures, consistent with the decrease in $D_n(B, T)$ shown in Figure 2. The table thus provides a compact numerical reference, complementary to the graphical results, for validating or parameterizing future experimental and simulation studies.

4. Conclusions

This study established a consistent analytical model linking internal transport parameters to the complex photocurrent of an n^+-p-p^+ silicon solar cell under modulated polychromatic illumination. Increasing the magnetic field reduces the longitudinal diffusion coefficient, whereas increasing temperature lowers mobility and weakens magnetic sensitivity. At 300 K, the model-defined 1% and 10% transport thresholds for D_n are 0.745 T and 2.469 T, respectively. However, these thresholds characterize internal transport rather than the electrical response directly. At $f = f_c$, a 1% reduction in D_n at 0.745 T produces only a 0.0858% decrease in photocurrent, whereas the electrical threshold $S_B = 1\%$ is reached near 2.61 T.

Within the magnetodiffusion mechanism considered here, environmental fields and fields below 100 mT produce negligible changes in D_n and in the calculated photocurrent. This conclusion does not exclude possible additional mechanisms that are not included in the model.

The frequency response also exhibits a reduction in magnitude and an increase in dynamic delay near and above f_c. Under the assumption that carrier lifetime is independent of magnetic field, the phase of the diffusion length remains independent of B, whereas the spatial profiles and photocurrent retain a thermomagnetic dependence through D_n and the boundary conditions. Finally, the complementary use of C_{TM}, S_B, and I_{TM} distinguishes the normalized magnetic response, the electrical threshold, and the intrinsic thermomagnetic interaction. Future work should incorporate a possible magnetic-field dependence of carrier lifetime, parasitic resistances and capacitances, and compare the predictions with frequency-domain measurements under a controlled magnetic field.

Author Contributions

- **Sada Traore** conceived the study, developed the theoretical model, performed the numerical simulations, analyzed and interpreted the results, prepared the figures, and wrote the original manuscript.
- **Moustapha Thiame** contributed to the method-ology, supervised the research, and critically revised the manuscript.
- **Seydou Faye and Landing Diatta** contributed to the interpretation of the results and reviewed the manuscript.

Conflicts of Interest

The authors declare no conflicts of interest regarding the publication of this paper.

References

[1] Rose, B.H. and Weaver, H.T. (1983) Determination of Effective Surface Recombination Velocity and Minority-Carrier Lifetime in High-Efficiency Si Solar Cells. *Journal of Applied Physics*, **54**, 238-247. https://doi.org/10.1063/1.331693

[2] Gaubas, E. and Vanhellemont, J. (1996) A Simple Technique for the Separation of Bulk and Surface Recombination Parameters in Silicon. *Journal of Applied Physics*, **80**, 6293-6297. https://doi.org/10.1063/1.363705

[3] von Roos, O. and Landsberg, P.T. (1985) Effect of Recombination on the Open-Circuit Voltage of a Silicon Solar Cell. *Journal of Applied Physics*, **57**, 4746-4751.

https://doi.org/10.1063/1.335339

[4] Schmidt, J. and Aberle, A.G. (1997) Accurate Method for the Determination of Bulk Minority-Carrier Lifetimes of Mono- and Multicrystalline Silicon Wafers. *Journal of Applied Physics*, **81**, 6186-6199. https://doi.org/10.1063/1.364403

[5] Dieng, A., Zerbo, I., Wade, M., Maiga, A.S. and Sissoko, G. (2011) Three-Dimensional Study of a Polycrystalline Silicon Solar Cell: The Influence of the Applied Magnetic Field on the Electrical Parameters. *Semiconductor Science and Technology*, **26**, Article 095023. https://doi.org/10.1088/0268-1242/26/9/095023

[6] Combari, D.U., Ramde, E.W., Sourabie, I., Zoungrana, M., Zerbo, I. and Bathiebo, D.J. (2018) Performance Investigation of a Silicon Photovoltaic Module under the Influence of a Magnetic Field. *Advances in Condensed Matter Physics*, **2018**, 1-8. https://doi.org/10.1155/2018/6096901

[7] Sun, J. and Kosel, J. (2013) Extraordinary Magnetoresistance in Semiconductor/Metal Hybrids: A Review. *Materials*, **6**, 500-516. https://doi.org/10.3390/ma6020500

[8] Alken, P., Thébault, E., Beggan, C.D., Amit, H., Aubert, J., Baerenzung, J., *et al.* (2021) International Geomagnetic Reference Field: The Thirteenth Generation. *Earth, Planets and Space*, **73**, Article No. 49. https://doi.org/10.1186/s40623-020-01288-x

[9] Mandelis, A. (1989) Coupled AC Photocurrent and Photothermal Reflectance Response Theory of Semiconducting p-n Junctions. I. *Journal of Applied Physics*, **66**, 5572-5583. https://doi.org/10.1063/1.343662

[10] Schinke, C., Hinken, D., Bothe, K., Ulzhöfer, C., Milsted, A., Schmidt, J., *et al.* (2011) Determination of the Collection Diffusion Length by Electroluminescence Imaging. *Energy Procedia*, **8**, 147-152. https://doi.org/10.1016/j.egypro.2011.06.116

[11] Honma, N. and Munakata, C. (1987) Sample Thickness Dependence of Minority Carrier Lifetimes Measured Using an Ac Photovoltaic Method. *Japanese Journal of Applied Physics*, **26**, Article 2033. https://doi.org/10.1143/jjap.26.2033

[12] Diao, A., Thiam, N., Zoungrana, M., Sahin, G., Ndiaye, M. and Sissoko, G. (2014) Diffusion Coefficient in Silicon Solar Cell with Applied Magnetic Field and under Frequency: Electric Equivalent Circuits. *World Journal of Condensed Matter Physics*, **4**, 84-92. https://doi.org/10.4236/wjcmp.2014.42013

[13] Diao, A., Wade, M., Thiame, M. and Sissoko, G. (2017) Bifacial Silicon Solar Cell Steady Photoconductivity under Constant Magnetic Field and Junction Recombination Velocity Effects. *Journal of Modern Physics*, **8**, 2200-2208. https://doi.org/10.4236/jmp.2017.814135

[14] Gueye, M., Diallo, H.L., Moustapha, A.K.M., Traore, Y., Diatta, I. and Sissoko, G. (2018) Ac Recombination Velocity in a Lamella Silicon Solar Cell. *World Journal of Condensed Matter Physics*, **8**, 185-196. https://doi.org/10.4236/wjcmp.2018.84013

[15] Traore, S., Diedhiou, A., Thiame, M., Tine, M., Camara, M. and Diatta, L. (2025) Dynamic Analysis of Thermomagnetic Effects on a $N^+/P/P^+$ Silicon Solar Cell. *Journal of Materials Science and Chemical Engineering*, **13**, 55-65. https://doi.org/10.4236/msce.2025.138005

[16] Ouedraogo, M., Traore, N.Y., Diasso, A., Sam, R. and Zougmore, F. (2025) Effect of Magnetic Field and Temperature on the Excess Minority Carrier Density in the Base of a Radial Junction Solar Cell. *Nano Select*, **6**, e70054. https://doi.org/10.1002/nano.70054

[17] Fossum, J.G. (1977) Physical Operation of Back-Surface-Field Silicon Solar Cells. *IEEE Transactions on Electron Devices*, **24**, 322-325. https://doi.org/10.1109/t-ed.1977.18735

[18] Shockley, W. and Read, W.T. (1952) Statistics of the Recombinations of Holes and Electrons. *Physical Review*, **87**, 835-842. https://doi.org/10.1103/physrev.87.835

[19] Jacoboni, C., Canali, C., Ottaviani, G. and Alberigi Quaranta, A. (1977) A Review of Some Charge Transport Properties of Silicon. *Solid-State Electronics*, **20**, 77-89. https://doi.org/10.1016/0038-1101(77)90054-5

[20] Sze, S.M. and Ng, K.K. (2007) Physics of Semiconductor Devices. Wiley. https://doi.org/10.1002/0470068329

[21] Sissoko, G., Museruka, C., Corréa, A., Gaye, I. and Ndiaye, A.L. (1996) Light Spectral Effect on Recombination Parameters of Silicon Solar Cell. *Renewable Energy*, **3**, 1487-1490.

[22] Diallo, H.L., Seïdou Maiga, A., Wereme, A. and Sissoko, G. (2008) New Approach of Both Junction and Back Surface Recombination Velocities in a 3D Modelling Study of a Polycrystalline Silicon Solar Cell. *The European Physical Journal Applied Physics*, **42**, 203-211. https://doi.org/10.1051/epjap:2008085

[23] Diasse, O., Diao, A., Wade, M., Diouf, M.S., Diatta, I., Mane, R., *et al.* (2018) Back Surface Recombination Velocity Modeling in White Biased Silicon Solar Cell under Steady State. *Journal of Modern Physics*, **9**, 189-201. https://doi.org/10.4236/jmp.2018.92012

[24] National High Magnetic Field Laboratory (MagLab) (2025) MagLab Sets a New World Record Magnetic Field (48.7 T). Florida State University.

[25] Hahn, S., Kim, K., Kim, K., Hu, X., Painter, T., Dixon, I., *et al.* (2019) 45.5-Tesla Direct-Current Magnetic Field Generated with a High-Temperature Superconducting Magnet. *Nature*, **570**, 496-499. https://doi.org/10.1038/s41586-019-1293-1

[26] Combari, D.U., Zerbo, I., Zoungrana, M., Ramde, E.W. and Bathiebo, D.J. (2017) Modelling Study of Magnetic Field Effect on the Performance of a Silicon Photovoltaic Module. *Energy and Power Engineering*, **9**, 419-429. https://doi.org/10.4236/epe.2017.98028

[27] Natural Environment Research Council (2026) British Geological Survey (BGS). The Earth's Magnetic Field: An Overview. https://geomag.bgs.ac.uk/education/earthmag.html

[28] Manso Jimeno, M., Vaughan, J.T. and Geethanath, S. (2023) Superconducting Magnet Designs and MRI Accessibility: A Review. *NMR in Biomedicine*, **36**, e4921. https://doi.org/10.1002/nbm.4921